Quantitative and qualitative study of density driven CO_2 mass transfer in a vertical Hele-Shaw cell

CrossMark

Titly Farhana Faisal [a], Sylvie Chevalier [a], Yves Bernabe [b], Ruben Juanes [b], Mohamed Sassi [a],*

[a] Masdar Institute of Science and Technology, P.O. Box 54224, Abu Dhabi, United Arab Emirates
[b] Massachusetts Institute of Technology, 77 Massachusetts Avenue, Building 48, Cambridge, MA 02139, USA

A B S T R A C T

The density driven convection phenomenon is expected to have a significant and positive role in CO_2 geological storage capacity and safety. But predictions on reservoir time and space scales are difficult to validate because data are generally sparse and will only be useful for a small part of the relevant time period. Laboratory scale data are valuable to validate the numerical models. In this paper we focus on the comparison of experimental and numerical determination of CO_2 mass transfer in a laboratory experiment. We developed an experimental protocol for the determination of density-driven mass transfer of CO_2 in water-saturated Hele-Shaw cells with different apertures. We used a CCD camera to capture images of the initiation of density-driven convection caused by dissolution of CO_2 in water and the subsequent development of convective fingers. The visualization of the phenomenon allowed consistently stopping the experiment when dissolved CO_2 first reached the bottom of the cell. We determined the total mass of dissolved CO_2 during the experiment using a catalytic combustion-based total carbon analyzer (TC-analyzer). This experimental procedure was repeated several times for uncertainty analysis. Thus a combination of quantitative and qualitative experimental results for the same Hele-Shaw cell configuration was obtained for validation of corresponding numerical simulation results. A numerical simulation of the phenomenon was carried out using the STOMP-WCS simulator. We found that in order to accurately simulate numerically the phenomenon occurring in the Hele-Shaw cell, existent variations in the cell apertures should be taken into account. Thus we observed a good agreement between the experimental and numerical results in terms of total dissolved CO_2 mass, timescale of mass transport and morphology of the convection fingers. In addition correlations are obtained between total dissolved CO_2 mass, arrival time of dissolved CO_2 to bottom of the cell, and the Rayleigh number.

© 2014 Elsevier Ltd. All rights reserved.

1. Introduction

Compared to the two other major geological storage options, namely, depleted hydrocarbon reservoirs and deep coal seams, deep saline aquifers have the highest potential global capacity for long-term CO_2 storage [1]. The Intergovernmental Panel on Climate Change (IPCC) Special CCS Report [2] states the global storage capacity estimate of saline aquifers to be from 1000 to 10,000 GT of CO_2, making them very attractive targets for large scale geological sequestration.

One of the fundamental physical phenomena related to CO_2 injection and storage in geological saline aquifers is the combination of dissolution, diffusion and convection of CO_2 in the brine-saturated rock formation [3]. Once the CO_2 is injected in

saline aquifer, the supercritical CO_2 being less dense than the brine rises up and forms a thin layer of free phase CO_2 underneath the formation seal. Dissolution of the free phase CO_2 in the brine and molecular diffusion of the dissolved CO_2 then begins. The CO_2 saturated brine is 0.1–1% denser than the original brine [4] depending on the pressure, temperature and salinity. Thus a gravitationally unstable system develops with a denser liquid overlying a more buoyant one, leading to gravitational convection of CO_2-rich liquid downward and CO_2-poor brine upward. Convection is a much faster transport process than molecular diffusion and is believed to play a key role in enhancing the dissolution of CO_2 ([5,6]). Of the four major trapping mechanisms [7]: (1) structural trapping, (2) capillary trapping, (3) dissolution trapping and (4) mineral trapping associated with geological sequestration of CO_2, the third one is greatly accelerated by convection thus significantly decreasing the potential for leakage of CO_2 and increasing the overall storage security. A significant convection phenomenon will result also in an enhanced CO_2 storage capacity of the reservoir.

---

* Corresponding author. Tel.: +971 28109148.
  E-mail address: msassi@masdar.ac.ae (M. Sassi).

Nomenclature

b	Hele-Shaw cell aperture		t_{conv}	onset time of convection
D	diffusion coefficient		t_s	first arrival time of dissolved CO_2 at the cell bottom
D_{Tay}	Taylor dispersion coefficient		U	average velocity in the flow direction
g	acceleration of gravity		$\mathbf{V}$	advective flux
h	diffusive layer thickness		V_{max}	maximum local velocity
h_c	pressure head difference between phases		W	Hele-Shaw cell width
H	Hele-Shaw cell height		$\mathbf{z}$	unit gravitation direction vector
$\mathbf{J}$	diffusive flux			
$\mathbf{k}$	intrinsic permeability		*Subscripts/superscripts*	
k_r	relative permeability		l	aqueous
m	Van Genuchten third parameter		g	gas
m_d	mass rate density		i	H_2O or CO_2
n	Van Genuchten second parameter			
M	molecular weight		*Greek symbols*	
M_{CO_2}	mass of dissolved CO_2		α	Van Genuchten first parameter
P	pressure		φ	porosity
Pe	Peclet number		γ	phase index (liquid or gaseous)
Ra	Rayleigh number		ρ	density
S	saturation		τ	tortuosity
S_{el}	effective water saturation		μ	dynamic viscosity
S_r	irreducible water saturation		ω	mass fraction
t	time		χ	mole fraction

Developing our understanding of this physical phenomenon so as to be able to predict the long-term field evolution with confidence is of crucial importance prior to widespread implementation of the sequestration technology. Given the large spatial and temporal scales involved, numerical modeling will most likely be the only practical approach. Much work has already been devoted to the numerical modeling of this dissolution–convection process [4–14].

Few of these studies combined experimental work with the numerical simulations. However, in order to build confidence in the modeling tools and/or gain physical knowledge to improve them, it is necessary to validate the numerical studies with experimental data. Neufeld et al. [3] concluded from their experimental and numerical work that dissolution in presence of density-driven convection should account for roughly 10% of the annually injected mass of CO_2. They highlighted the lack of quantification of CO_2 mass storage due to convection as a function of average reservoir properties. Further experimental and numerical studies in this area include work by [4,11,13–19]. Particularly, Kneafsey and Pruess [4] performed experiments in transparent vertical Hele-Shaw cells and established a very successful protocol for visualization of density driven convection patterns of dissolved CO_2 in water. They also did numerical simulations for qualitative comparison with the experimental configurations using TOUGH/ECO2N achieving reasonable agreement with certain discrepancies in timescales and overall pattern. Quantitative determination of the total dissolved CO_2 mass has not been done experimentally for this Hele-Shaw cell configuration. However Kneafsey and Pruess [20] briefly introduced a quantitative approach to determine dissolved CO_2 as a function of time by measuring pressure decline in a pressurized cylindrical experimental setup. The cylindrical vessel contained porous media (of varying grain sizes) saturated with brine and the limited headspace over the medium was filled with CO_2 gas under pressure. Similar experimental vessels measuring mass transfer of CO_2 using the pressure decay concept was used by Farajzadeh et al. [18] and Yang and Gu [21]. But visualization of the convection/dissolution was of course not possible for these setups.

In this study we focused on (1) the experimental work required to obtain combination of quantitative and qualitative data for the CO_2 dissolution–convection phenomenon and on (2) the comparison between experimental and numerical results. Our first objective was to develop an experimental protocol to determine the total mass of dissolved CO_2 during the visualized convection process in the Hele-Shaw cell. To ensure the visibility and repeatability of our experiments we followed the protocol developed by Kneafsey and Pruess [4] to visualize density driven convection of dissolved CO_2 in transparent Hele-Shaw cells. Thus we are able to compare not only convection pattern and timescales but also total dissolved mass of CO_2 with numerical simulations performed using STOMP (Subsurface Transport Over Multiple Phases) developed by the PNNL (Pacific Northwest National Laboratory) Hydrology group of the Department of Energy, USA. This paper is organized as follows: the experimental protocol and numerical methodology are explained in Sections 2 and 3 respectively. Results and discussions are presented in Section 4 followed by summary and conclusions in Section 5.

2. Experimental methods and procedures

2.1. Experimental setup

Fig. 1 features the basic experimental setup and relevant procedure consisting of the Hele-Shaw cell and the connections to the total dissolved CO_2 mass determination and convection pattern visualization sections respectively. As illustrated, transparent Hele-Shaw cells were constructed by assembling two glass plates (20 cm by 30 cm) parallel to each other with a known separation, b. The separation is precisely controlled by use of pencil lead spacers (with b much smaller than the other dimensions of the cell) [4]. The vertical and bottom sides of the cells were sealed with silicon. The internal cell dimensions were W = 15 cm and H = 28 cm for the length and height, respectively. The height of water column only is 22 cm.

The main purpose of Hele-Shaw cells is to simulate an environment mathematically analogous to 2D flow in porous media [4,22,23]. The flow equations which are used for the Hele-Shaw
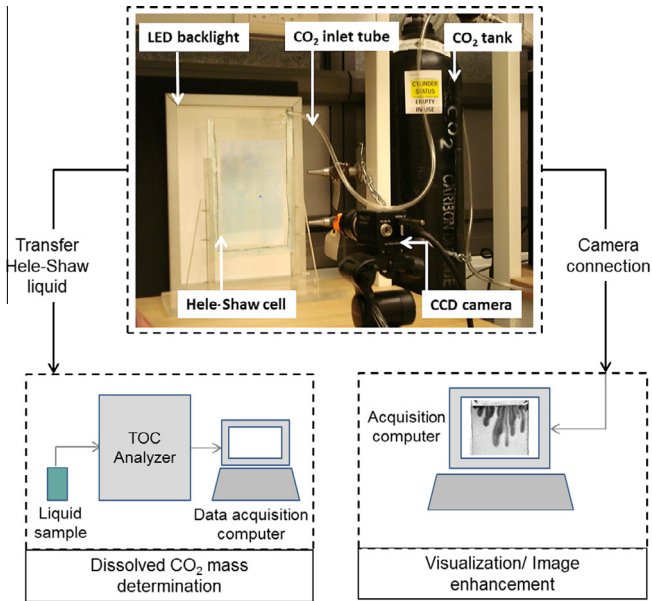
Fig. 1. The basic experimental setup consisting of the Hele-Shaw cell with schematic connections to (bottom-left): experimental configuration for determination of total dissolved CO_2 mass and (bottom-right): experimental configuration for image processing and enhancement of captured convection patterns.

model are derived from the Navier–Stokes equations [24]. Integrating these equations over the saturated domain with respect to y from 0 to b leads to formulations that are comparable to Darcy's Law in a 2D homogeneous porous media in which the permeability is related to the cell aperture as following:

$$k = \frac{b^2}{12} \qquad (1)$$

Cell apertures of 0.3, 0.5, 0.7 and 1 mm were used. The corresponding permeabilities and Rayleigh numbers were calculated assuming uniform aperture (Table 1). The Rayleigh number is a dimensionless number expressing the ratio of free convection to diffusion and is defined as shown in Eq. (2):

$$Ra = \frac{\Delta \rho g k H}{\mu D \varphi} \qquad (2)$$

where, $\Delta \rho$ is the increase in water density due to dissolution of CO_2 [kg/m^3], g the acceleration of gravity [m/s^2], H is the height of the column of water inside the cell [m], D the molecular diffusion coefficient of CO_2 in water [m^2/s], μ the dynamic viscosity of water [kg/(s m)], k the permeability of the porous medium [m^2] and φ the porosity (in our case, $\varphi = 1$).

Theoretical studies showed that natural convection becomes preponderant when the Rayleigh number Ra is greater than a critical value equal to $4\pi^2$ [4,26]. Experiments were designed to meet this criterion in all cases.

The main limitation of the Hele-Shaw cell analogy is the restriction to a 2D flow geometry, wherein lateral dispersion or instabilities pertaining to a three-dimensional medium cannot be

considered [27]. Fernandez et al. [15] asserted that it could be possible to find a criterion to determine whether the concentration gradient following the gap-direction is negligible, depending on the interface thickness. They found that for $Ra_b \leqslant O(10^2)$ (see Eq. (3)), the Hele-Shaw analogy should remain valid.

$$Ra_b = \frac{\Delta \rho g b^3}{12 \mu D} \qquad (3)$$

Calculating Ra_b values corresponding to our experimental configurations (Table 2), we found that Ra_b for $b = 1$ mm Hele-Shaw cell reaches the order of the limit mentioned in [15] meaning that there may be a concentration gradient in the gap direction. However based on the work done by Oltean et al. [25] we calculated the maximum local Peclet numbers (Eq. (4)) for $b = 1$ mm configuration. As the maximum local velocity could not be measured experimentally, the velocity data obtained from the numerical simulations was used (Table 3).

$$Pe = \frac{V_{max} b}{D} \qquad (4)$$

where V_{max} is the maximum local velocity (m/s).

Oltean et al. [25] found in their work that the analogy is valid for Pe < 50 [25]. Based on our Pe values we assume that even if the numerical V_{max} is only an estimate of the experimental V_{max}, we are in the limit of the validity and that the 3D effects that may occur will remain negligible.

Notice that the aperture of the cell is not truly constant. Careful observation of the top edge of the cell showed that the aperture was non-uniform with a greater gap near the center. The aperture variations are due to the flatness defects of the glass surfaces. These local changes in aperture are important since they directly influenced the permeability field in the cell and consequently affect the convection pattern.

The experiments were conducted at room temperature (22 °C) and atmospheric pressure. CO_2 gas was introduced at the top of the vertical Hele-Shaw cell (filled with water to a marked level of height, H) using a thin needle inserted between the two plates. This needle was connected to the CO_2 tank via a tube and a pressure regulator. The flow rate of CO_2 injected was adjusted by means of the pressure regulator so as to be just enough to generate a steady stream of bubbles when the needle was immersed in a beaker of water. Minimizing the flow rate was important to avoid disturbing the water interface at the top of the cell. CO_2 is denser than air (the molecular weights of CO_2 and air are 44 g/mol and 29 g/mol, respectively) and, therefore, settles over the water–gas interface by replacing the air, which is free to escape from the unsealed top. At first, CO_2 dissolves at the water–CO_2 interface via molecular diffusion then propagates downwards within the Hele-Shaw cell via density driven convection. Dissolution of CO_2 produces a slight density increase of water. The higher density of the CO_2-rich water at the top of the cell leads to a gravitational instability and consequently to the formation of convective fingers.

Following Kneafsey & Pruess's [4] visualization technique, the dissolved CO_2 convective fingers can be visualized using a pH tracking dye solution of bromocresol green. Owing to the high sensitivity of the dye to pH changes, a number of precautions

Table 1
The cell aperture thickness for four experiments with corresponding average permeability and Rayleigh number assuming uniform aperture thickness.

b [mm]	k [m^2]	Ra [–]
1	8.33×10^{-8}	36420.87
0.7	4.08×10^{-8}	17846.22
0.5	2.08×10^{-8}	9105.22
0.3	7.5×10^{-9}	3277.88

Table 2
Ra_b values for cells $b = 1$, 0.7, 0.5 and 0.3 mm to check validity of Hele-Shaw cell analogy as 2D porous medium.

b [m]	Ra_b [–]
0.001	165
0.0007	57
0.0005	21
0.0003	4.5

Table 3
Maximum local Peclet number for cell $b = 1$ mm to check validity of Hele-Shaw cell analogy as 2D porous medium. The local velocity data is obtained from the numerical simulations presented in Section 4.4.

b [m]	V_{max} [m/s]	Pe [–]
0.001	6.6×10^{-5}	44

had to be taken, (a) systematic use of de-ionized water, (b) a waiting time of at least a week to allow complete curing of the standard architectural grade silicon used for sealing the cell and avoid contamination by acetic acid. We used both dry and wet curing, by leaving the cell dry for about 4–5 days and then saturated with water for another 3–4 days.

During the course of experiments, we noted that the position and orientation of the injection needle had a significant influence on both the initiation of convection and the long term convection pattern. We performed a series of identical visualization experiments except for the position and orientation of the injection needle. Three needle orientation and positions were tested: (1) vertical needle located at center of cell-top, (2) vertical needle located at side of cell-top, and (3) slanted needle at about 15° with the needle head located at cell-top-center. Results showed that both configurations (1) and (2) introduced external effects in pattern and hence were difficult to reproduce during repetitions (e.g. case 1 generated a single finger while case 2 produced a dissymmetric biased distribution of fingers). Configuration (3) caused the least disturbance [28]. This configuration provided the greatest reproducibility of the experiments.

Thus using the needle configuration 3), experiments were repeated at least three times for the cells with the largest cell volume (b equal to 1 and 0.7 mm) in order to determine the average arrival time t_s needed for the first dissolved CO_2 finger to reach the bottom of the cell. Fig. 2 shows examples of three separate runs in identical conditions demonstrating the relatively good reproducibility of the experiments in terms of the timescale t_s.

2.2. Determination of the mass of dissolved CO_2

In order to determine the total mass of CO_2 dissolved in the cell (M_{CO_2}) at the characteristic time t_s, the experiments were stopped when dissolved CO_2 first reached the bottom of the cell. Based on the relatively good reproducibility in timescale as shown in Fig. 2, all experiments were stopped at time t_s for consistency.

To maximize accuracy, only the large volume cells ($b = 1$ and 0.7 mm) were used for measuring the total mass of dissolved CO_2. Moreover for the 0.5 and 0.3 mm cells, due to strong capillary effects it was difficult to recover the entire volume of the liquid as quickly and carefully as the larger cells. In each of these experiments the volume of liquid recovered after emptying cell was precisely measured. The mean values for time scale t_s and the liquid volume recorded for repeated experiments (minimum three repetitions) with the two cells are reported below in Table 4.

At t_s, the CO_2 supply was closed. The liquid contained in the Hele-Shaw cell at time t_s was quickly and carefully transferred to a 150 ml bottle containing 100 ml of pre-made solution of sodium hydroxide (pH~14). The bottle top was then sealed and stoppered. The bottle content was profusely shaken to ensure uniform mixing. The sodium hydroxide solution was used for two reasons. Firstly this increases the pH of the solution and converts the dissolved CO_2 to more stable carbonate and bicarbonates, hence preventing loss of CO_2 from the solution when in the bottle [30,31]. Secondly the addition of 100 ml of sodium hydroxide solution dilutes the carbon content to levels (from 0 to 100 ppm) consistent with the calibration curve used by the TOC-L analyzer.

The diluted liquid in the bottle was analyzed for total carbon (TC) using a 680 °C catalytic combustion method by means of a Shimadzu TOC-L analyzer [29]. The thin sample extraction tube of the TOC-L analyzer was inserted through the bottle's seal layer. The liquid sample was subjected to combustion in an oxygen-rich environment in tubes filled with platinum catalyst. The CO_2 generated during combustion is cooled, dehumidified and finally measured by a high-sensitivity infrared gas analyzer (NDIR). The detection sensitivity limit is 4 µg/l (the highest level for catalytic combustion method available today) [29]. The corresponding total carbon mass is calculated based on preliminary calibration curve data.

Before running the actual experiments, calibration test runs were performed using bicarbonate solutions of known TC concentrations to test the accuracy and precision of the values reported by the TOC-L analyzer. For three different TC concentrations the experimental error in the reported average TC value was found to be less than 3%. Experiments were repeated three times for each sample concentration giving a standard error of ±0.5 ppm.

Since the tube connecting the TOC-L analyzer to the sample bottle was possibly contaminated by residues of the solution previously analyzed, we repeated the TC measurement 6 times for each liquid sample. The first run having been discounted, a stabilization of the TC values for the consequent 5 runs was observed. The average of the last 5 values was used as a measure of the total carbon content in the solution and the corresponding mass of dissolved CO_2 was computed from it. Nonetheless this value needed to be corrected for some additional sources of experimental error as described below.
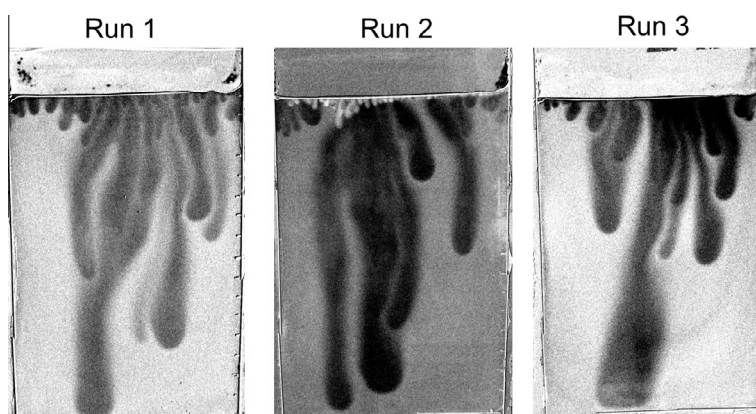
Fig. 2. Three visualization results for the $b = 0.7$ mm cell at 113 min showing good reproducibility both in terms of timescale t_s and overall convection pattern.

Table 4
The mean time when dissolved CO_2 first reached cell bottom and mean volume of the liquid inside cells for b = 1 and b = 0.7 mm.

	b = 1 mm	b = 0.7 mm
Mean time t_s when dissolved CO_2 first reached cell bottom (min)	83	113
Mean volume of liquid recovered after emptying the cell (ml)	43	32

One problem arose from unpreventable exposure to the atmosphere of the stored sodium hydroxide solution before it was added in the TC analyzer. That is, while the sodium hydroxide was trapping the dissolved CO_2 from escaping, it was also adding excess CO_2 from atmosphere. Thus TC measurements of the amount of atmospheric CO_2 dissolved in the sodium hydroxide solution were made prior to each experiment and background corrections were determined. We minimized subsequent exposure to the atmosphere by not only sealing the bottle instantly but also performing the TC analysis quickly, within less than ten minutes after the running the Hele-Shaw experiments.

As the operational TOC machine was able to generate results for the total carbon (TC) only i.e. organic and inorganic carbon were not reported separately, an additional protocol had to be integrated to correct for excess organic carbon introduced due to bromocresol green dye. For that we made preliminary TC measurements of the freshly prepared, initial solution (1:30 volumetric ratio of bromocresol green and water). Since the exact volume of solution was known for each experiment, the excess carbon content caused by bromocresol green could be subtracted from the TC measurements. We verified the validity of this correction by comparing the corrected results to those obtained in identical experimental conditions but without bromocresol green. Thus a total of 6 experiments were performed for each cell: 3 with the dye and 3 without. Since visualization of the convection fingers was impossible without the dye, we stopped these tests at the same times t_s that were used to stop the corresponding experiments with the dye.

2.3. Image capture and enhancement methodology

The geometry of the convection fingers is captured at regular intervals using the SONY XCL-5005CR Color PoCL (Power over Camera Link) Camera equipped with Navitar 5 megapixel and 12 mm lens. This high resolution camera has a 2/3 progressive scan CCD sensor with square pixels and can capture 15 frames per second. The camera is connected to an image acquisition computer, with the necessary software installed (PIXCI EB1P Frame Grabber from EPIX Inc. and the image processing software XCAP-Std V3.7). To avoid external reflections, the experiments were conducted in a dark room where the uniform LED table was the only source of light.
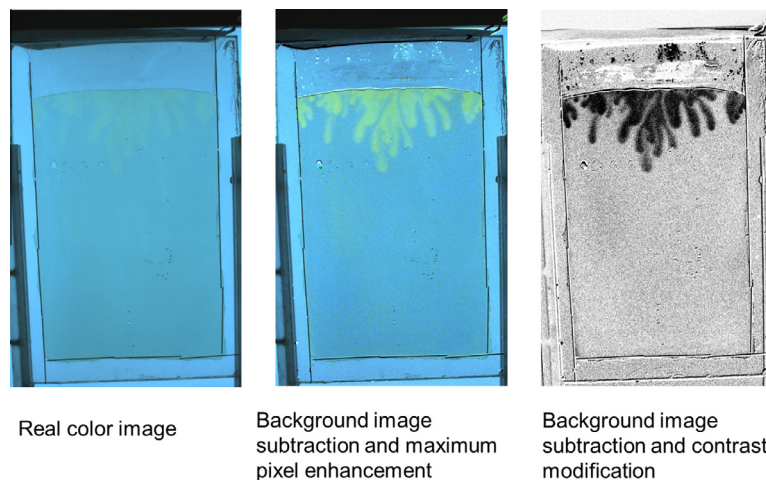
Even though the dyed fingers were visible to naked eye, they did not appear distinctly enough in the original color images and image enhancement had to be performed. Accordingly, we recorded a background image of the set-up taken before convection started. Once CO_2 was introduced and convection began, we subtracted the background image from all subsequent images in order to isolate the changes due to convection. Of course, it is imperative to ensure that the set-up remains in the same position during this whole procedure. Further enhancement after background image subtraction involved maximizing the pixel values to amplify the pixel colors. We also found it more visually appealing to convert the images to grayscale format and invert them such that the originally light fingers appear dark. Fig. 3 shows example of such cases.

3. Numerical model

3.1. Numerical model formulation

The physical model used in our simulations was built similar to the experimental configuration considering a pure CO_2 gas layer at the top of the Hele-Shaw cell (Fig. 4). Simulations were performed using STOMP (Subsurface Transport Over Multiple Phases) [32]. In STOMP, the solution of the discretized governing equations is based on the integral volume finite difference method. STOMP is a sequential numerical simulator which allows the user to choose the solved governing equations and their related state equations. For the present work, the governing equations presented below correspond to the STOMP Operational mode STOMP-WCS (Water–CO_2–Salt) even though no brine was considered in this study.

The conservation equations of water and CO_2 masses is expressed in Eq. (5) where water and CO_2 are assumed to exist in aqueous (l) and gas (g) phases under equilibrium conditions.

| Real color image | Background image subtraction and maximum pixel enhancement | Background image subtraction and contrast modification |

Fig. 3. Illustrating effect of image enhancement compared to (left): real color image before any correction, (middle): image after background subtraction and pixel enhancement, (right): image after background subtraction followed by contrast modification in grayscale. (For interpretation of the references to color in this figure legend, the reader is referred to the web version of this article.)
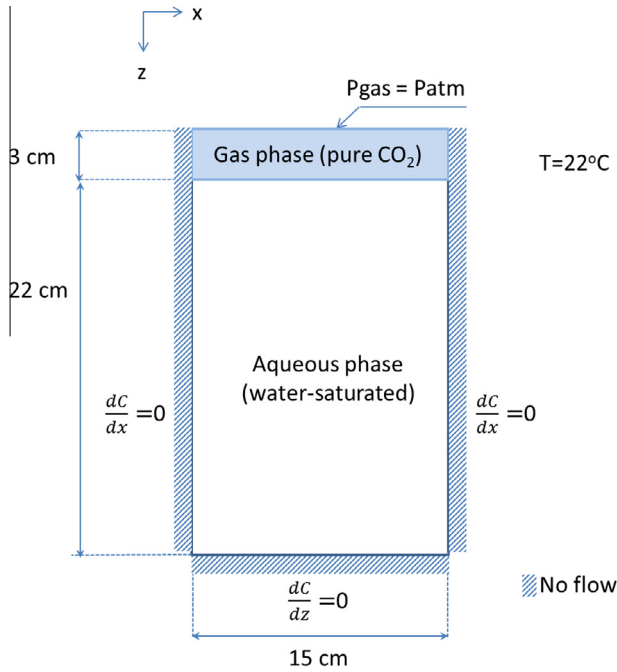
Fig. 4. Physical model.

$$\frac{\partial}{\partial t}\left[\sum_{\gamma=l,g}\left(\phi\rho_\gamma S_\gamma \omega_\gamma^i\right)\right] = -\sum_{\gamma=l,g}\nabla\left(\rho_\gamma \omega_\gamma^i \mathbf{V}_\gamma\right) - \sum_{\gamma=l,g}\nabla\left(\mathbf{J}_\gamma^i\right) + \sum_{\gamma=l,g}\left(\omega_\gamma^i m_{d\gamma}\right) \tag{5}$$

where i represents H_2O or CO_2; γ the liquid or gaseous phase; ϕ (–) the porosity, ρ (kg/m^3) the density, S (–) the saturation, ω (–) the mass fraction, m_d (kg/sm^3) the mass rate density.

The advective fluxes $\mathbf{V}_\gamma$ (m/s) of the mobile phases are computed according to the Darcy's law (for $\gamma = l, g$):

$$\mathbf{V}_\gamma = -\frac{k_{r\gamma}\mathbf{k}}{\mu_\gamma}\left(\nabla P_\gamma + \rho_\gamma g\mathbf{z}\right) \tag{6}$$

where k_r is relative permeability, $\mathbf{k}$ intrinsic permeability (m^2), μ (Pa s) dynamic viscosity, P (Pa) pressure and g (m/s^2) acceleration of gravity.

The diffusive fluxes $\mathbf{J}$ (kg/m^{3}s) are computed considering molecular diffusion but ignoring mechanical dispersion (for $\gamma = l, g$):

$$\mathbf{J}_\gamma^i = -\phi\rho_\gamma S_\gamma \frac{M^i}{M_\gamma}\left(\tau_\gamma D_\gamma^i\right)\nabla\chi_\gamma^i \tag{7}$$

where M (kg/kmol) is molecular weight, τ (–) tortuosity, D (m^2/s) diffusion coefficient and χ (–) mole fraction. Note that $\tau = 1$ as we are using the Hele-Shaw cell analogy.

A detailed description of all the state equations used in STOMP-WCS can be found in White et al. [32]. The state equations adopted in the present work are those proposed by [33] for phase equilibria, [34] for aqueous density and [35] for viscosity. Aqueous density and viscosity are dependent on the CO_2 properties and the concentration of dissolved CO_2 in the aqueous phase. Henry's law is used to compute the CO_2 dissolution in water following [36]. Computation of the aqueous molecular diffusion of CO_2 is based on the approach developed by Renner [37].

The physical conditions and fluid properties as computed in STOMP-WCS are summarized in Table 5.

To close the system and simulate the multiphase transfer in the porous medium representing the Hele-Shaw cell, a saturation function as well as the air- and water-relative permeability relationships should be defined in STOMP. The saturation function plays the

Table 5
Fixed conditions and calculated fluid properties.

Temperature	22 °C
Pressure (top)	1.013 bar
Salinity	No salt
Dissolved CO_2 mass fraction at saturation	1.533×10^{-3}
Water dynamic viscosity	0.95475×10^{-3} Pa s
Dynamic viscosity variation[a] (decrease[b])	2.5×10^{-6} Pa s (0.26%)
Water density	997.95 kg/m^3
Density variation[a] (increase[b])	0.29 kg/m^3 (0.029%)
Diffusion coefficient of dissolved CO_2 in pure water	1.4424×10^{-9} m^2/s
Diffusion coefficient variation[a] (increase[b])	5.7×10^{-12} m^2/s (0.4%)

[a] Difference between pure water and water saturated by dissolved CO_2.
[b] Increase means that the property of pure water is lower than the one of water saturated by dissolved CO_2.

role of a boundary condition and does not affect the validity of the Hele-Shaw cell analogy in the aqueous phase. To represent adequately the experimental configuration, the saturation function has to maximize the sharpness of the interface between the liquid and gas phases. A Van Genuchten [38] saturation function (Eq. (8)) with very high parameter values ($\alpha = 1000$; $n = 7$) associated with two Mualem relative permeability functions [39,40] for the gas and aqueous solutions (Eq. (9)) is appropriate for this purpose. With this model, we obtained aqueous saturations varying from 1 to less than 10^{-3} in 1 mm across the liquid/gas interface.

Van Genuchten [38] demonstrated the ability of the following analytical expression between the aqueous saturation S_l (–) and the pressure head difference between phases h_c (m) to predict the hydraulic conductivity of unsaturated soils:

$$S_l = (1 - S_r)\left[1 + (\alpha h_c)^n\right]^{-m} + S_r \tag{8}$$

S_r (–) is the irreducible water saturation; α (1/m), n (–) and $m = 1 - 1/n$ are the Van Genuchten parameters and $h_c = h_g - h_l$ (m) is the pressure head difference between phases.

The aqueous and gas relative permeabilities vary with the water saturation according to:

$$k_{rl} = (S_{el})^{1/2}\left[1 - \left(1 - (S_{el})^{1/m}\right)^m\right]^2 \text{ and } k_{rg}$$
$$= (1 - S_{el})^{1/2}\left[1 - \left(1 - (S_{el})^{1/m}\right)^m\right]^2 \tag{9}$$

where $S_{el} = (S_l - S_r)/(1 - S_r)$ is the effective water saturation.

3.2. Boundaries and initial conditions

For the 2D computations, the boundary and initial conditions simulated the experimental ones. The flow domain was initially at hydrostatic pressure and room temperature. No-flow conditions are imposed for the bottom and lateral boundaries. The presence of a 3 cm-high layer of CO_2 gas overlaying the aqueous-saturated part of the domain was considered (multiphase model) and the top boundary condition of the domain consists of an atmospheric gas pressure condition. We checked that beyond 3 cm increasing the thickness of the CO_2 gas layer does not induce any significant difference (<1%) in the M_{CO_2} results. In order to induce the convection phenomenon, we chose to include small sinusoidal perturbations (10^{-4} to 10^{-6} in dissolved CO_2 saturation), in the initial condition (at time $t = 0$) instead of using numerical rounding errors to trigger the instabilities [13]. The perturbations were located just below the interface with the gas phase where the saturation of dissolved CO_2 is 1.

3.3. Permeability fields

Since the permeability is proportional to the square of the cell aperture, a small variation in aperture should affect the flow phenomenon. Discrepancies between experimental and numerical results should arise when these aperture variations (mentioned in Section 2.1) are not included in the simulations.

We measured the aperture variations using the method of Detwiler et al. [41]. We measured the light intensity transmitted through the transparent Hele-Shaw cell filled with water and normalized the results with respect to the light intensity measured in absence of a cell. The normalized light intensity varies with the cell aperture fluctuations. Combining the light intensity data with a few direct aperture measurements in discrete locations can be transformed into aperture fields and the corresponding permeability fields (Fig. 5a and b). The method was sufficiently accurate to numerically estimate the effect of permeability heterogeneities.
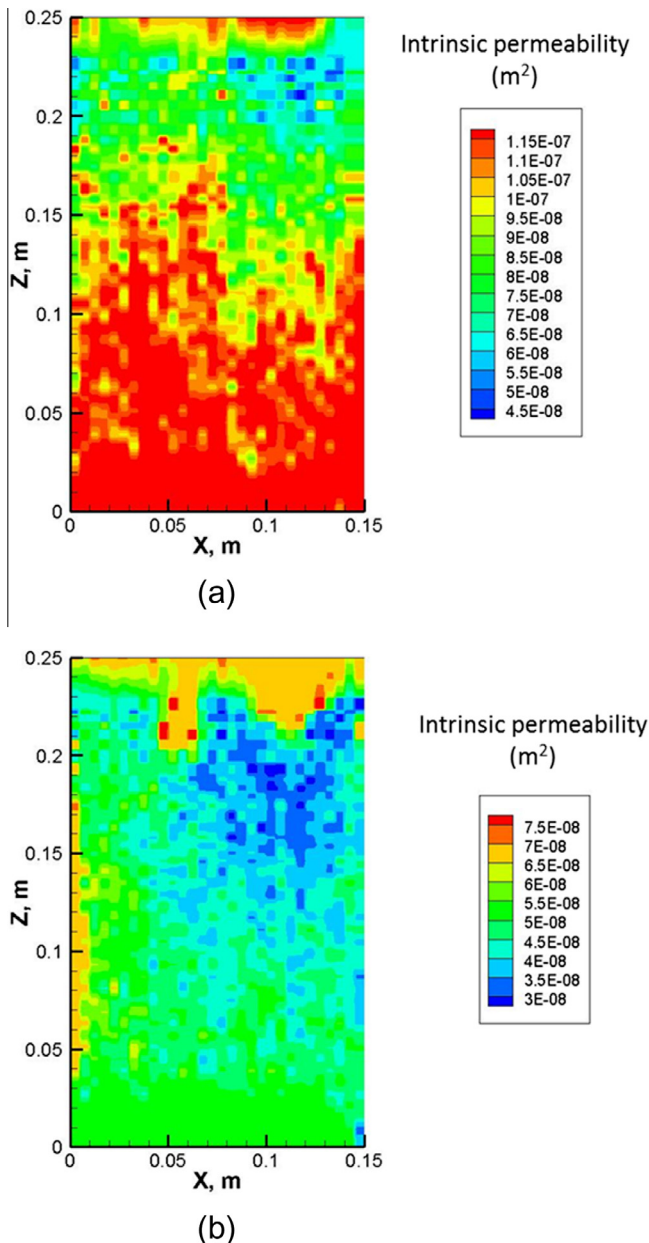

(a)

(b)

Fig. 5. Permeability fields resulting from the transmitted light analysis on the two experimental Hele-Shaw cell configurations: (a) 1 mm gap and (b) 0.7 mm gap.

The permeability fields corresponding to the Hele-Shaw cells of Table 1 are shown in Fig. 5a and b.

3.4. Numerical considerations

The computational domain was discretized on a non-uniform mesh of 150×212 (grid cell length of 1 mm, minimal grid cell height equal to 0.05 mm). Grid cells were refined vertically in the region of the gas/water interface (where CO_2 dissolution occurs and convection fingering process initiates). Space discretization near the gas/water interface should effectively be smaller than the expected diffusive layer thickness [42]. Time steps were controlled through the respect of a Newton–Raphson convergence criterion equal to 10^{-6}, with a maximum value of 0.1 s.

A number of simulations were carried out with increasing grid resolutions and decreasing convergence criterion and maximum time step values in order to check for grid convergence issues. Results were analyzed at the first arrival time of dissolved CO_2 at the bottom of the cell. These computational domain characteristics were considered optimal since the use of more refined meshes or lower criteria did not lead to significant differences in the total mass of dissolved CO_2 (variations remained inferior to 1%). These total dissolved CO_2 mass computations confirmed the suitability of the 150×212 mesh for accurate simulation of the density driven convection phenomenon. We also analyzed the effect of the small sinusoidal perturbations included in the initial conditions. At small magnitudes (10^{-4} to 10^{-6}), these perturbations did not induce any significant changes (mass variations remain less than 2%) on the dissolved CO_2 mass transfer.

4. Results and discussion

The main aim of this experimental work was to develop a protocol for determination of total mass of dissolved CO_2 during a visible density-driven convection process inside a Hele-Shaw to offer a more concrete quantitative comparison with numerical simulations. Since our comparisons with numerical simulation require both qualitative convection pattern and quantitative t_s and M_{CO_2}, our experimental results consist of both parts.

4.1. Experimental visualization (b = 1, 0.7, 0.5 and 0.3 mm)

Permeability was varied by changing the cell aperture b. Likewise the characteristic dimensionless numbers Pe and Ra were directly related to b. Our results are reported below in decreasing order of cell aperture (or, equivalently, in decreasing order of Ra, Pe and cell permeability). All images were processed as discussed in Section 2.3.

Fig. 6 shows successive snapshots for the cell with $b = 1$ mm. The process was rather fast, with small fingers forming within the first minute of the experiment. With time, the fingers tended to coalesce into a few longer and thicker ones. As mentioned in Section 2.1, the cell aperture was smaller near the sides of the cell, perhaps explaining the lower growth rate of the fingers there. The dissolved CO_2 first reached the cell bottom at $t_s = 83 \pm 1$ min.

Similar sequences of images were observed for the other experiments (shown in Figs. 7–9 corresponding to $b = 0.7$, 0.5 and 0.3 mm, respectively). Table 6 shows t_s and corresponding Rayleigh numbers. The main difference is that the finger growth rate decreases as b (or, equivalently, the Rayleigh number Ra) is reduced. This is in agreement with Riaz et al. [7], who stated that the finger interactions are more vigorous for larger Rayleigh numbers. We again observed a preferential growth of the fingers near the central axis of the cell, possibly corresponding to a larger aperture in this region. This larger aperture region was measured for
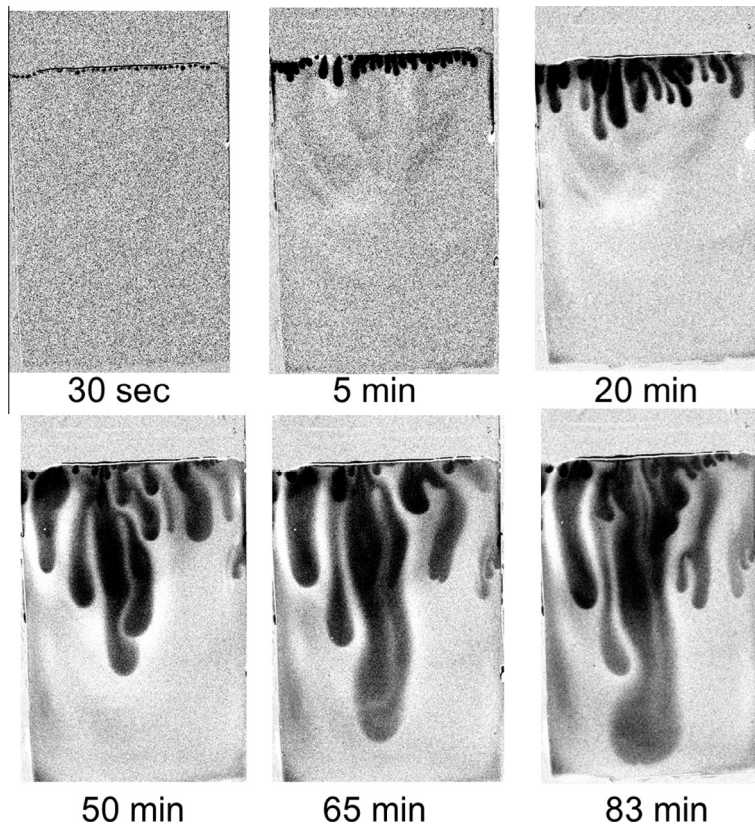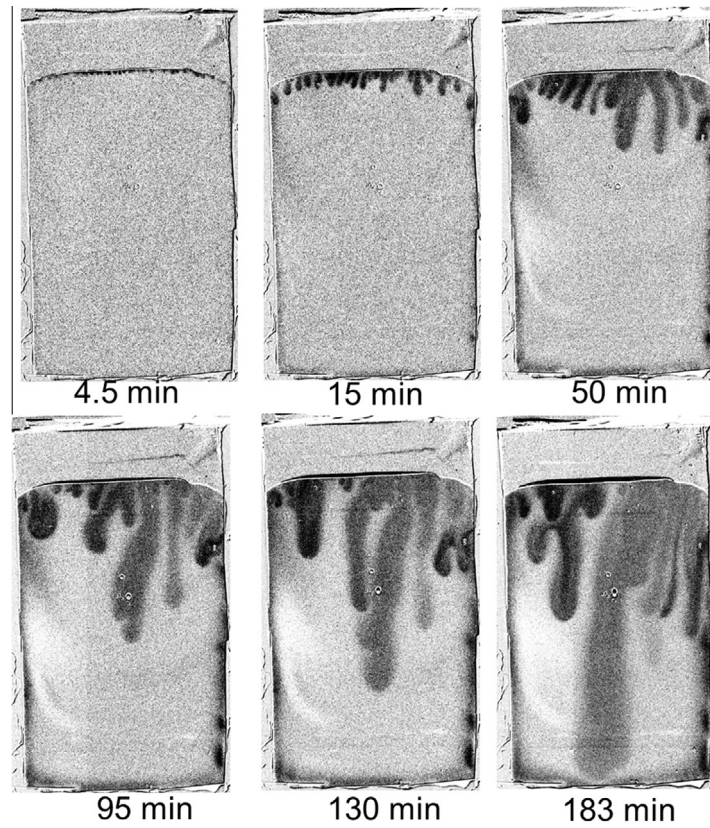
Fig. 6. Enhanced experimental images at progressing time shots of density-driven CO_2 convection finger advancement in water for parallel plate aperture $b = 1$ mm (Rayleigh number ≈ 36400).
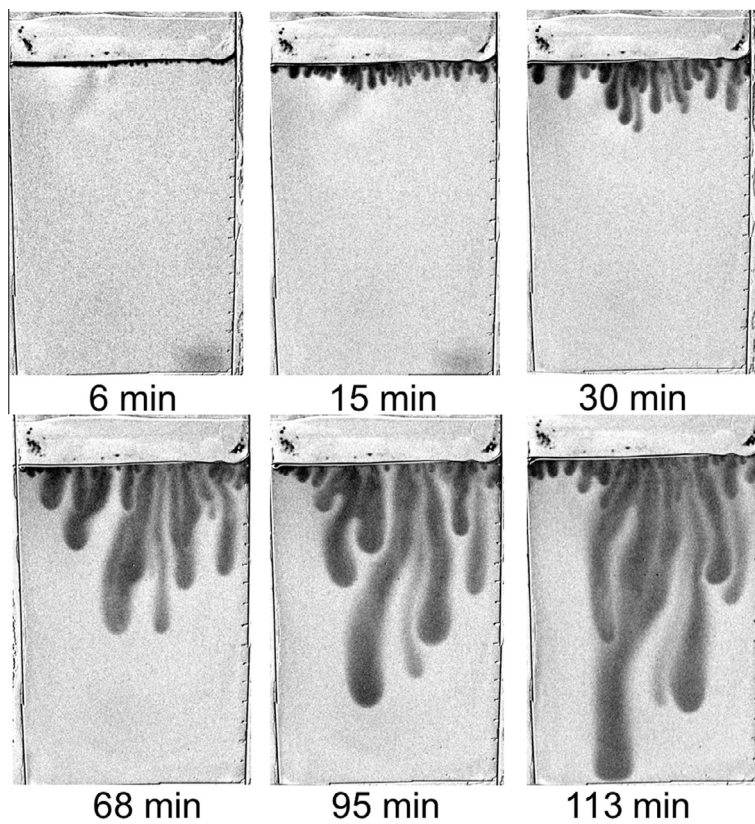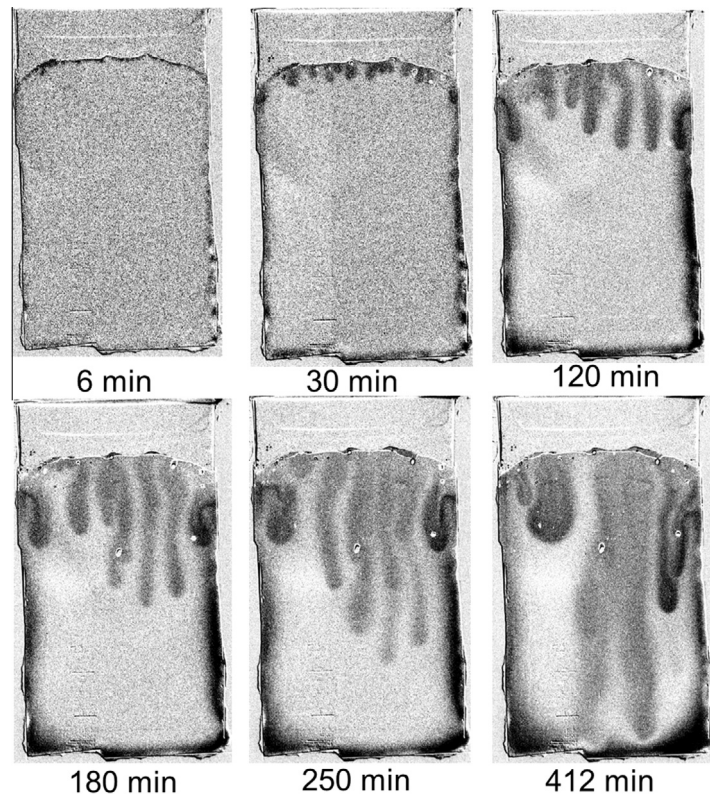

Fig. 7. Enhanced experimental images at progressing time shots of density-driven CO_2 convection finger advancement in water for parallel plate aperture of $b = 0.7$ mm (Rayleigh number ≈ 17800).

Fig. 8. Enhanced experimental images at progressing time shots of density-driven CO_2 convection finger advancement in water for parallel plate aperture of b = 0.5 mm (Rayleigh number $\approx$ 9100).

Fig. 9. Enhanced experimental images at progressing time shots of density-driven CO_2 convection finger advancement in water for parallel plate aperture of b = 0.3 mm (Rayleigh number $\approx$ 3200).

Table 6
Rayleigh numbers, Ra for the four Hele-Shaw cells and corresponding times taken for first dissolved CO_2 to reach cell bottom, t_s.

Ra [−]	t_s [min]
36420.87	83
17846.22	113
9105.22	183
3277.88	412

cells $b = 1$ and 0.7 mm experimentally. At the top of the cells, the largest aperture values were 1.1 and 0.85 mm for the two cells respectively. However we note that for the $b = 0.5$ and 0.3 mm cells (Figs. 8 and 9 respectively), the inclination of the water surface suggests a decrease of capillary pressure at the cell sides and therefore a greater aperture since water is the wetting fluid.

4.2. Experimental total mass of dissolved CO_2 (b = 1 and 0.7 mm)

As described in Section 2.2, the total carbon content (in ppm or mg/l) of the cell liquid at time t_s was measured and corrected for organic carbon from Bromocresol Green and excess inorganic carbon from atmospheric CO_2 due to addition of sodium hydroxide. The corrected value was then converted into an equivalent mass of CO_2, M_{CO_2} (in kg), by using the molecular weight ratio of both species. The measured TC values for each experiment and the corresponding calculated M_{CO_2} are reported in Table 7 (refer to Section 2.2 for accuracy and precision of reported TC readings). The relative error of the M_{CO_2} between two experiments may exceed 13% as can be seen from Table 7. As shown in Fig. 2 the experiments have a good repeatability on timescale and patterns. However the inherent instable nature of the dissolution/convection process causes the amount of dissolved CO_2 mass during each experiment to vary. Therefore the 13% error includes not only the uncertainties due to CO_2 mass measurements but also uncertainties due to non-perfect repeatability of the instability itself. Moreover, the relative error of M_{CO_2} between experiments may have been reduced if we chose to stop each experiment by observing when dissolved CO_2 first reached the bottom of the cell. But mass calculation in experiments without Bromocresol would have not been achievable.

We note that a higher measured TC did not necessarily correspond to a higher M_{CO_2} in all cases because the TC contributions of the dye and/or sodium hydroxide solution were not always the same. Our results also indicate that the dye (at the dilution ratio that we have used) does not have any effect on the convection/dissolution process of CO_2 in water. The relative difference between the average M_{CO_2} values determined with and without bromocresol green is less than 1%.

As expected we found that M_{CO_2} increased with increasing cell aperture thickness b and, therefore, increasing permeability and Rayleigh number. These results are presented graphically in

Table 7
Measured TC [ppm] and corresponding mass of dissolved CO_2, M_{CO_2} [kg] values for cells $b = 1$ and 0.7 mm for 6 experiments per cell. 3 experiments were conducted with dye and 3 without.

	Measured TC in solution without dye [ppm]	Corresponding calculated M_{CO_2} [kg]	Measured TC in solution with dye [ppm]	Corresponding calculated M_{CO_2} [kg]
$b = 1$ mm	11.34	5.17×10^{-6}	15.78	5.04×10^{-6}
	11.51	5.25×10^{-6}	16.63	5.42×10^{-6}
	10.31	4.62×10^{-6}	15.55	4.67×10^{-6}
$b = 0.7$ mm	7.87	3.22×10^{-6}	12.43	3.03×10^{-6}
	7.75	3.08×10^{-6}	11.87	2.97×10^{-6}
	7.98	2.74×10^{-6}	11.02	3.09×10^{-6}
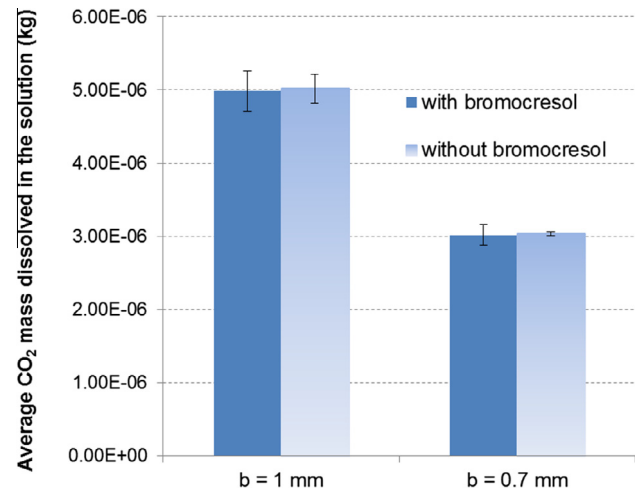
Fig. 10. Column chart representation of average total mass of dissolved CO_2 during the Hele-Shaw experiments for $b = 1$ and 0.7 mm cells. The columns show experimental masses for both with and without bromocresol green dye indicating the standard error margin for each case.

Fig. 10 including the standard experimental errors for the measured mass.

4.3. Relationship between Rayleigh number and arrival time

For our experiments we used four Hele-Shaw cells with different Rayleigh numbers (Table 1). It is of interest to note the influence of the Rayleigh number on this density driven mass transfer of CO_2.

Farajzadeh et al. [11] analyzed similar results in log–log scale for their single phase numerical simulations (see Fig. 9 in [11]). For their simulation conditions they found a linear relationship between the Rayleigh number and inverse of the dimensionless time needed for the dissolved CO_2 to reach bottom. In Fig. 11 we plot in log–log scale the dimensionless experimental arrival time for first dissolved CO_2 to reach bottom (t_s) versus the different Rayleigh numbers. We use the dimensionless time, $\tau = (D/H^2)t_s$ as defined in [11] for the sake of comparison. The portion of Farajzadeh et al.'s [11] numerical results corresponding to our range of data is copied in Fig. 11.

Our results indicate that t_s and Ra have a power relationship of the following form (Eq. (10)) when Ra is expressed as a function of t_s.
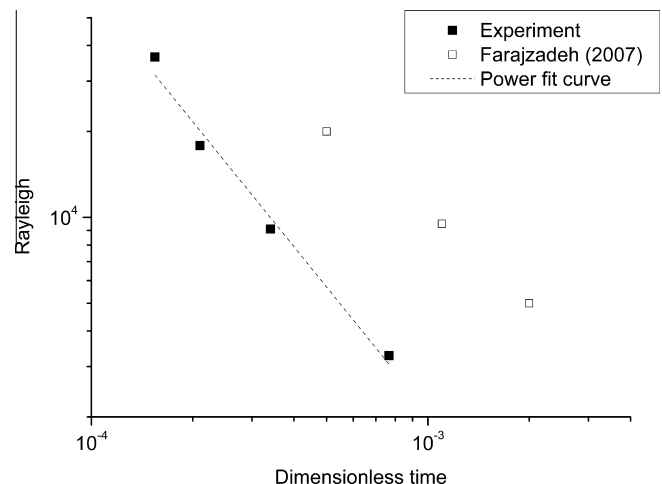
Fig. 11. Rayleigh numbers for four Hele-Shaw cells against the dimensionless experimental time for the first dissolved CO_2 to reach the cell bottom (t_s) in log–log scale compared with Fig. 9 in Farajzadeh et al. [11].

$$Ra = c \cdot t_s^{-n} \tag{10}$$

where c is a constant and n is the exponent with values of $c = 0.0891$ and $n = 1.45$ compared to $n = 1$ in [11].

Potential 3D effects (Section 2.1) from the highest Ra cell do not affect our data set significantly. Analyzing only the three lowest Ra data points, we found $n = 1.305$. This value is still not close to $n = 1$ which is not surprising as Farajzadeh et al. [11] state that their obtained relation depends on the specific conditions of their simulations. The numerical assumptions including the use of single

phase boundary conditions in their simulations may have contributed towards this difference.

4.4. Comparison between experimental and numerical results (b = 1 and 0.7 mm)

One of the main objectives of this experimental study was to validate the numerical simulation tools to be used later in field applications. Figs. 12 and 13 compare the convection fingers of the numerical simulations to the experimental ones in identical
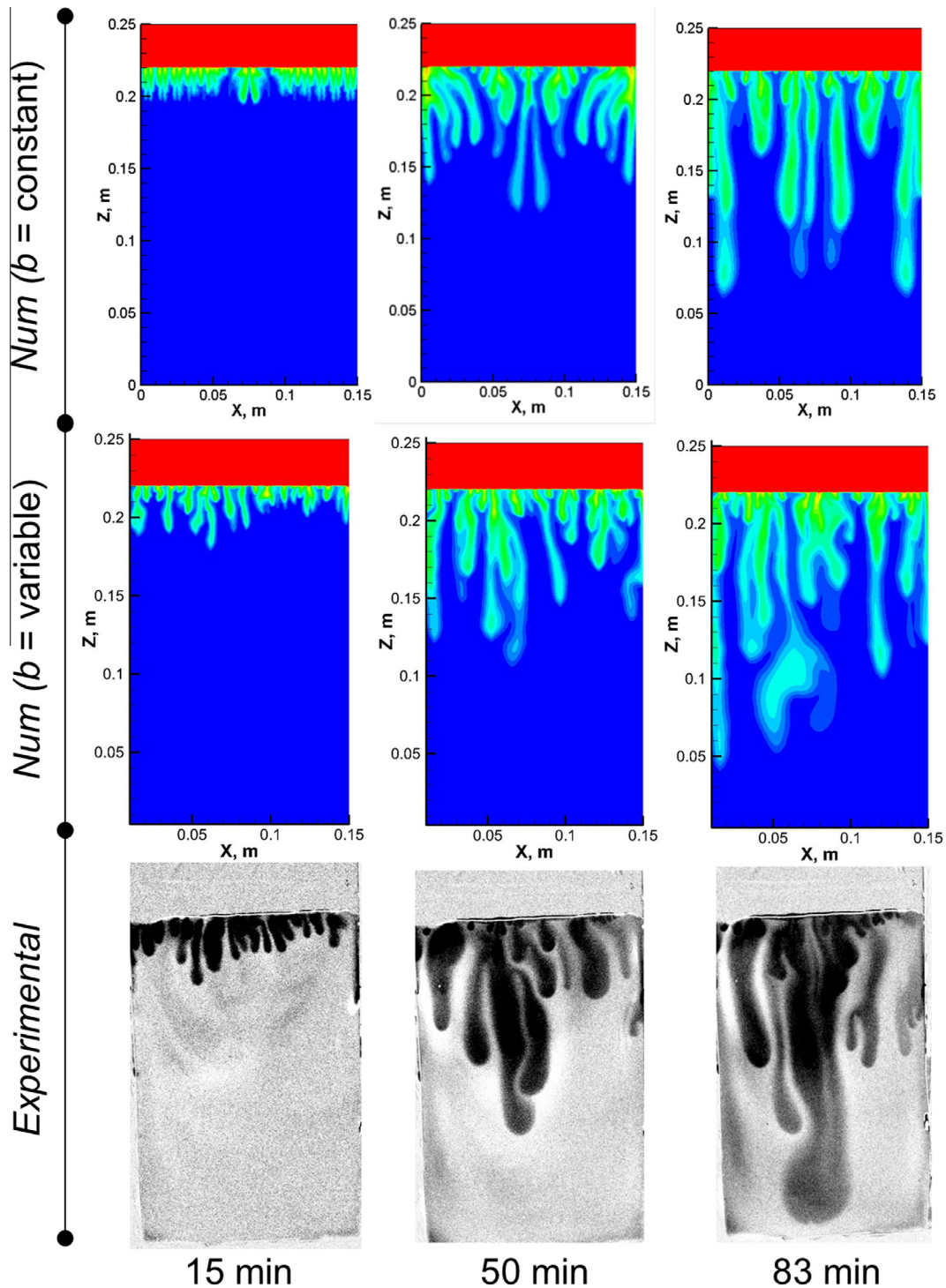
Fig. 12. Evolution of dissolved CO_2 fingers for the $b = 1$ mm cell for experimentally observed enhanced images (bottom row) vs. numerical with constant aperture (top row) and with variable apertures (middle row) at times: 15, 50, and 83 min.
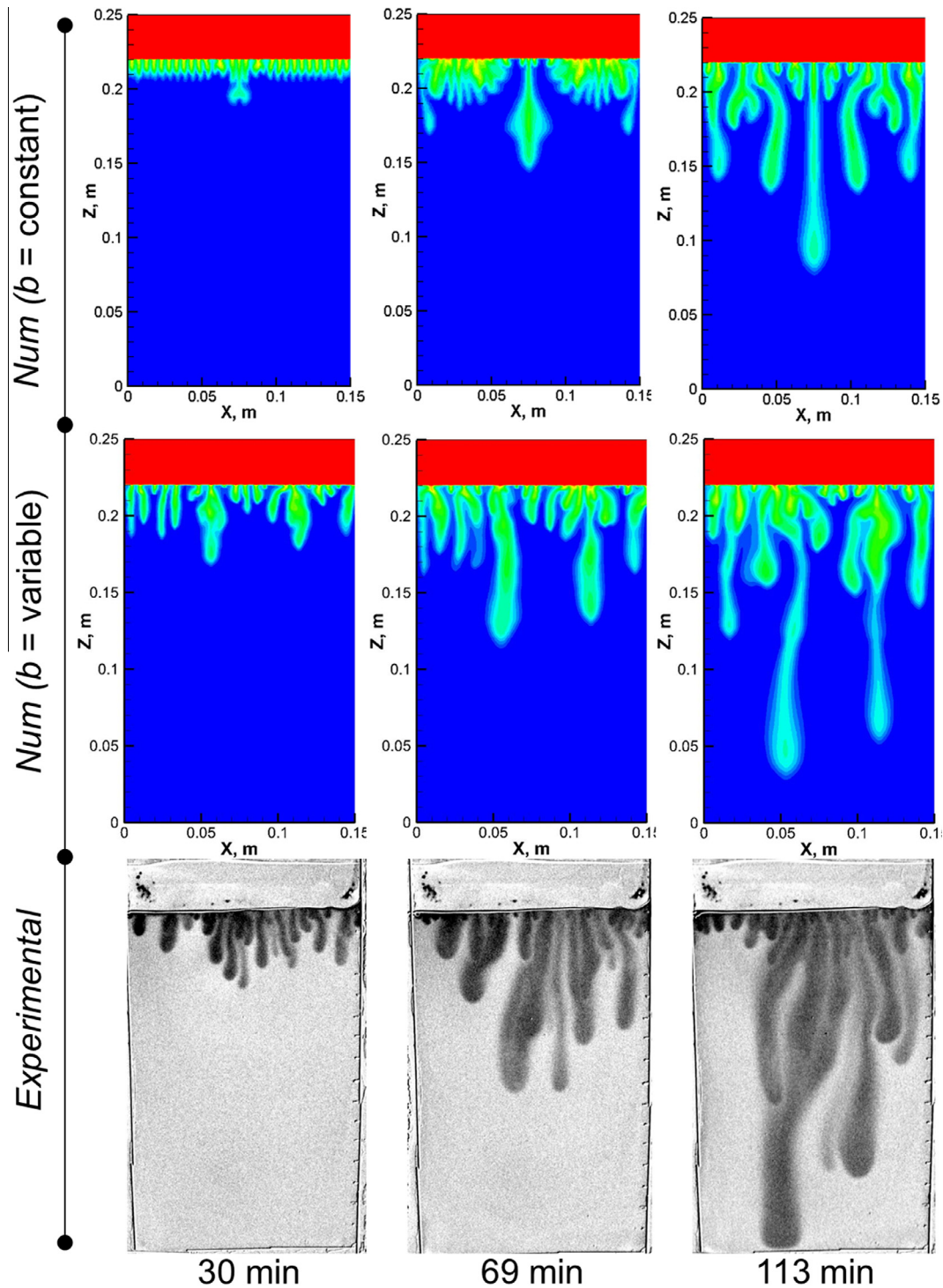
Fig. 13. Evolution of dissolved CO_2 fingers for the $b = 0.7$ mm cell for experimentally observed enhanced images (bottom row) vs. numerical with constant aperture (top row) and with variable aperture (middle row) at times: 30, 69, and 113 min.

conditions and times, for uniform permeability fields corresponding to constant aperture and for heterogeneous permeability fields corresponding to the aperture variations that have been measured (Section 3.3). Note that in the overlaying gas phase, even though the aqueous saturation is negligible, the dissolved CO_2 saturation appearing in simulation results is equal to 1. Including the heterogeneous permeability fields in the computations has improved the timescale comparison with experiments. It also contributes to improve simulations of the fingering morphology as they are in

better agreement with the experimental fingering morphology. For both cells the experimental convection patterns were asymmetrical, a feature well reproduced numerically when measured aperture variations are included in the simulations. Variations of the cell aperture obviously explain experimental observations such as preferential fingering phenomenon in the central part of the cell, and reduced experimental timescales.

However, for all simulation configurations, the characteristic timescales t_s at which dissolved CO_2 first reached the bottom of

the cell were still slightly larger than the experimental t_s. For the configuration of an average aperture equal to 1 mm, the numerical timescale decreases to 99 min (b variable) instead of 102 min (b constant) versus 83 min for the experimental one. The improvement is more obvious in the configuration of an average aperture equal to 0.7 mm, for a numerical timescale of 136 min (b variable) instead of 245 min (b constant) versus 113 min for the experimental one. The remaining timescale discrepancy can be partly explained by the precision of the Hele-Shaw cells reference aperture measurements (+/−0.1 mm).

Fig. 14 compares M_{CO_2}, the total mass of dissolved CO_2 at time t_s, for the different configurations. The inclusion of aperture variations in the simulation contributes noticeably to a better agreement between numerical and experimental results for both setups. The difference between the experimental and numerical M_{CO_2} for the constant aperture case is reduced by 36.5% (for $b = 1$ mm) and 54.8% (for $b = 0.7$ mm) for the variable aperture simulation. The relative differences of the experimental and numerical M_{CO_2} values remained however 25.3% and 29% for the cells with average $b = 1$ mm and average $b = 0.7$ mm, respectively. The numerical simulations also overestimated M_{CO_2}, the total mass of dissolved CO_2 when compared at experimental timescale t_s ($t_s = 83$ and 113 min for the two cases shown in Fig. 15, with $b = 1$ and 0.7 mm, respectively). At these times, the relative differences of the experimental and variable aperture numerical M_{CO_2} values were 14.4% and 21% for the cells with $b = 1$ and 0.7 mm, respectively.

Several reasons can be attributed to this discrepancy. Some loss of CO_2 during the sample transfer for the TC measurements may occur despite quick transfers and addition of sodium hydroxide since the set-up was not completely isolated from the surroundings. However the good repeatability of the tests assures that such losses were minimal and controlled. Moreover, CO_2 loss alone cannot be sufficient to explain such discrepancies. More important factors such as the uncertainty associated to the permeability field and modeling assumptions used for the gas/water interface are most likely to contribute to such discrepancy.

We tested different boundary conditions for the gas/water interface (single phase and a dissolved CO_2 saturation equal to one (as in [11,14]), a layer of partial gas saturation (as in [4]); a partial saturation in dissolved CO_2 and an unsaturated media at the top of the domain). In particular single phase simulations leads to strong overestimations of the CO_2 mass transfer (numerical val-
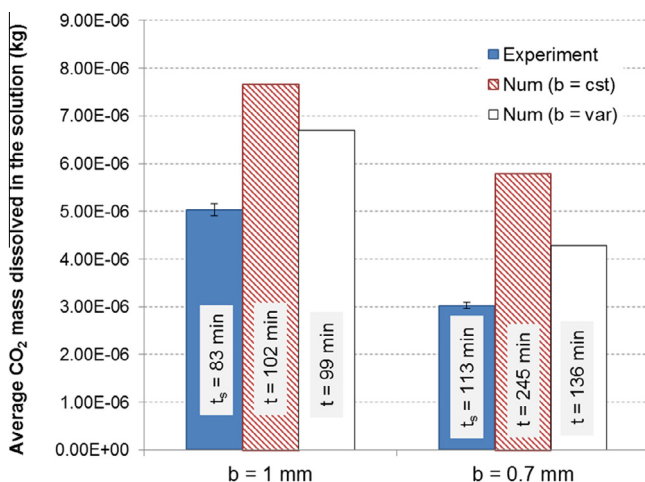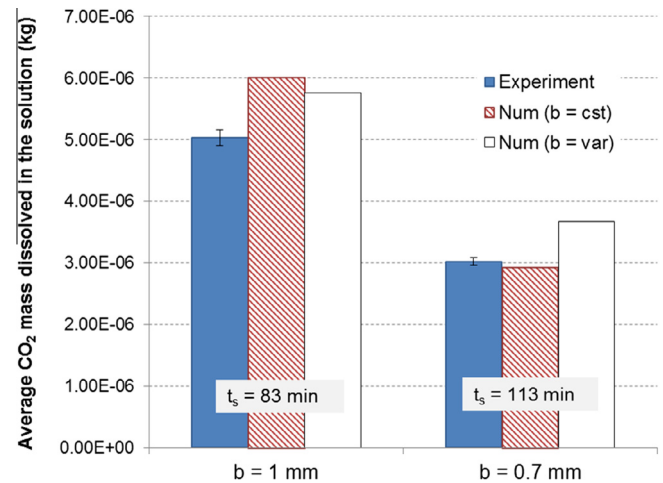

Fig. 15. Column chart representation of average total mass of dissolved CO_2 for $b = 1$ and 0.7 mm cells. Average mass from experiments (with standard error margin) is compared with that from simulations at the same time as that of the experimental t_s i.e. 83 min (for $b = 1$ mm) and 113 min (for $b = 0.7$ mm).

ues reach 3 to 5 times the experimental values of dissolved CO_2 mass). The unsaturated media definition was chosen to optimize both mass transfer and the timescale results compared to experimental data. However the mass transfer and timescale are still overestimated by the numerical simulations. The main reason is because the presence of the transition zone at the interface slows down the phenomenon. Thus comparison of the total mass of dissolved CO_2 at t_s leads to a better fit between experimental and numerical mass results (compare Figs. 14 and 15).

5. Conclusions

Experiments of density-driven mass transfer of CO_2 in water were performed in Hele-Shaw cells with different apertures. During the course of the experiments we took successive snapshots of the convection process, allowing characterization of the convection morphology and timescales. The experiments were stopped when dissolved CO_2 first reached the bottom of the cell. We determined the total mass of dissolved CO_2 during the experiment. We have successfully developed an original protocol for the measurement of total dissolved CO_2 mass resulting from density driven mass transfer of CO_2 in a vertical Hele-Shaw cell. This has allowed us to extend the qualitative visualization analysis of the density driven convection phenomenon to a quantitative analysis offering a more concrete ground of comparison between experimental and numerical simulation results.

The obtained experimental and numerical results are found to be in relatively good agreement in terms of timescales (numerical results overestimate by 20%) and overall convection fingering patterns. Simulations were found to over-predict the total mass of CO_2 by 25% to 29%. Taking into account the experimental cell aperture variations was very important for obtaining more accurate simulation of the CO_2 mass transfer timescale and magnitude. Modeling assumptions used for the gas/water interface contribute to these remaining discrepancies. Experimental data analysis showed power correlations between arrival time of CO_2 to cell bottom and the Rayleigh number.

Fig. 14. Column chart representation of average total mass of dissolved CO_2 for $b = 1$ and 0.7 mm cells. Average mass from experiments (with standard error margin) is compared with that from simulations at the corresponding first arrival times of dissolved CO_2 at the cell bottom.

Conflict of interest

None declared.

Acknowledgments

References

[1] K. Michael, M. Arnot, P. Cook, J. Ennis-King, R. Funnell, J. Kaldi, D. Kirste, L. Paterson, CO2 storage in saline aquifers I – current state of scientific knowledge, Energy Procedia 1 (2009) 3197–3204. Proceedings of the GHGT-9 Conference.

[2] B. Metz, O. Davidson, H.C. de Coninck, M. Loos, L.A. Meyer, (Eds.), IPCC special report on carbon dioxide capture and storage, in: Prepared by Working Group III of the Intergovernmental Panel on Climate Change Cambridge University Press, Cambridge and New York, NY, 2005, 442 pages.

[3] J.A. Neufeld, M.A. Hesse, A. Riaz, M.A. Hallworth, H.A. Tchelepi, H.E. Huppert, Convective dissolution of carbon dioxide in saline aquifers, Geophys. Res. Lett. 37 (2010) L22404.

[4] T.J. Kneafsey, K. Pruess, Laboratory flow experiments for visualizing carbon dioxide-induced density-driven brine convection, Transp. Porous Media 82 (2010) 123–139.

[5] G.S.H. Pau, J.B. Bell, K. Pruess, A.S. Almgren, M.J. Lijewski, K. Zhang, High-resolution simulation and characterization of density-driven flow in CO_2 storage in saline aquifers, Adv. Water Resour. 33 (2010) 443–455.

[6] A.C. Slim, T.S. Ramakrishnan, Onset and cessation of time-dependent dissolution-driven convection in porous media, Phys. Fluids 22 (2010) 124103.

[7] A. Riaz, M. Hesse, H.A. Tchelepi, F.M. Orr, Onset of convection in a gravitationally unstable diffusive boundary layer in porous media, J. Fluid Mech. 548 (2006) 87–111.

[8] J. Ennis-King, L. Paterson, Role of convective mixing in the long-term storage of carbon dioxide in deep saline formations, Soc. Petrol. Eng. J. 10 (3) (2005) 349–356.

[9] X. Xu, S. Chen, D. Zhang, Convective stability analysis of the long-term storage of carbon dioxide in deep saline aquifers, Adv. Water Resour. 29 (2006) 397–407.

[10] S. Ghanbari, Y. Al-Zaabi, G.E. Pickup, E. Mackay, F. Gozalpour, A.C. Todd, Simulation of CO_2 storage in saline aquifers, Chem. Eng. Res. Des. 84 (A9) (2006) 764–775.

[11] R. Farajzadeh, H. Salimi, P.L.J. Zitha, H. Bruining, Numerical simulation of density-driven natural convection in porous media with application for CO_2 injection projects, Int. J. Heat Mass Transfer 50 (2007) 5054–5064.

[12] C. Green, J. Ennis-King, K. Pruess, Effect of vertical heterogeneity on long-term migration of CO_2 in saline formations, Energy Procedia 1 (2009) 1823–1830. Proceedings of the GHGT-9 Conference.

[13] J.J. Hidalgo, J. Carrera, Effect of dispersion on the onset of convection during CO_2 sequestration, J. Fluid Mech. 640 (2009) 441–452.

[14] R. Farajzadeh, P. Ranganathan, P.L.J. Zitha, J. Bruining, The effect of heterogeneity on the character of density-driven natural convection of CO_2 overlying a brine layer, Adv. Water Resour. 34 (2011) 327–339.

[15] J. Fernandez, P. Kurowski, P. Petitjeans, E. Meiburg, Density-driven unstable flows of miscible fluids in a Hele-Shaw cell, J. Fluid Mech. 451 (2002) 239–260.

[16] S.E. Pringle, R.J. Glass, C.A. Cooper, Double-diffusive finger convection in a Hele-Shaw cell: an experiment exploring the evolution of concentration fields, length scales and mass transfer, Transp. Porous Media 47 (2002) 195–214.

[17] B. Arendt, D. Dittmar, R. Eggers, Interaction of interfacial convection and mass transfer effects in the system CO_2–water, Int. J. Heat Mass Transfer 47 (2004) 3649–3657.

[18] R. Farajzadeh, A. Barati, H.A. Delil, J. Bruining, P.L.J. Zitha, Mass transfer of CO_2 into water and surfactant solutions, Pet. Sci. Technol. 25 (12) (2007) 1493–1511.

[19] R. Farajzadeh, P.L.J. Zitha, H. Bruining, Enhanced mass transfer of CO_2 into water: experiment and modeling, Ind. Eng. Chem. Res. 48 (2009) 6423–6431.

[20] T.J. Kneafsey, K. Pruess, Laboratory experiments and numerical simulation studies of convectively enhanced carbon dioxide dissolution, Energy Procedia 4 (2011) 5114–5121. Proceedings of the GHGT-10 Conference.

[21] C. Yang, Y. Gu, Accelerated mass transfer of CO_2 in reservoir brine due to density-driven natural convection at high pressures and elevated temperatures, Ind. Eng. Chem. Res. 45 (2006) 2430–2436.

[22] T. Nguyen-Quang, H. Nguyen, F. Guichard, A. Nicolau, G. Szatmari, G. LePalec, M. Dusser, J. Lafossee, J.L. Bonnet, J. Bohatier, Two-dimensional gravitactic bioconvection in a protozoan (Tetrahymena pyriformis) culture, Zoolog. Sci. 26 (2009) 54–65.

[23] A.V. Gorin, On analogy between convective heat and mass transfer processes in a porous medium and a Hele-Shaw cell, Heat Mass Transfer Porous Media 13 (2012) 139–159.

[24] D. Todd, Unsteady flow in porous media by means of a hele-shaw viscous fluid model, EOS Transactions American Geophysical Union 35 (6) (1954) 905–916.

[25] C. Oltean, F. Golfier, M.A. Bues, Experimental and numerical study of the validity of Hele-Shaw cell as analogue model for variable-density flow in homogeneous porous media, Adv. Water Resour. 31 (2008) 82–95.

[26] E. Lindeberg, D. Wessel-Berg, Vertical convection in an aquifer column under gas cap of CO_2, Energy Convers. Manage. 38 (1997) S229–S234.

[27] D.A. Nield, A. Bejan, Convection in Porous Media, fourth ed., Springer, New York, 2006, pp. 44–45.

[28] T.F. Faisal, S. Chevalier, M. Sassi, Experimental and numerical studies of density driven natural convection in saturated porous media with application to CO_2 geological storage, Energy Procedia 37 (2013) 5323–5330. Proceedings of the GHGT-11 Conference.

[29] Shimadzu Scientific Instrument. TOC Analyzer TOC-L series: 680 °C combustion catalytic oxidation method measurement principles. Retrieved from Shimadzu: <http://www.ssi.shimadzu.com/products/product.cfm?product=toc-l4> (Accessed 2012 December).

[30] J.R. Bastidas-Oyanedel, Z. Mohd-Zaki, S. Pratt, J.P. Steyer, D.J. Batstone, Development of membrane inlet mass spectrometry for examination of fermentation processes, Talanta 83 (2010) 482–492.

[31] C.N. Sawyer, P.L. McCarty, G.F. Parkin, Chemistry for Environmental Engineering and Science, fifth ed., McGraw Hill, New York, 2003. pp. 572.

[32] M.D. White, D.J. Watson, D.H. Bacon, S.K. White, B.P. McGrail, Z.F. Zhang, STOMP, subsurface transport over multiple phases, STOMP-CO2 and -CO2e Guide, PNNL-21268, U.S. department of ENERGY, 2012, 270 pages.

[33] N. Spycher, K. Pruess, J. Ennis-King, CO_2–H_2O mixtures in geological sequestration of CO_2. I. Assessment and calculation of mutual solubilities from 12 to 100 °C and up to 600 bar, Geochimica and Cosmoschimica Acta 67 (16) (2003) 3015–3031.

[34] G. Alendal, H. Drange, Two-phase near-field modeling of purposefully released CO_2 in the ocean, J. Geophys. Res. 106 (C1) (2001) 1085–1096.

[35] A. Kumagai, C. Yokoyama, Viscosities of aqueous NaCl solutions containing CO_2 at high pressures, J. Chem. Eng. Data 44 (1999) 227–229.

[36] A. Battistelli, C. Calore, K. Pruess, The simulator TOUGH2/EWASG for modelling geothermal reservoirs with brines and noncondensible gas, Geothermics 26 (4) (1997) 437–464.

[37] T.A. Renner, Measurement and correlation of diffusion coefficients for CO_2 and rich-gas applications, SPE Reservoir Eng. (1988) 517–523.

[38] M.Th. Van Genuchten, A closed-form equation for predicting the hydraulic conductivity of unsaturated soils, Soil Sci. Soc. Am. J. 44 (1980) 892–898.

[39] Y. Mualem, A new model for predicting the hydraulic conductivity of unsaturated porous media, Water Resour. Res. 12 (3) (1976) 513–522.

[40] L. Luckner, M.Th. Van Genuchten, D.R. Nielsen, A consistent set of parametric models for the two-phase flow of immiscible fluids in the subsurface, Water Resour. Res. 25 (10) (1989) 2187–2193.

[41] R.L. Detwiler, S.E. Pringle, R.J. Glass, Measurement of fracture aperture fields using transmitted light: an evaluation of measurement errors and their influence on simulations of flow and transport through a single fracture, Water Resour. Res. 35 (9) (1999) 2605–2617.

[42] K. Pruess, Numerical modeling studies of the dissolution–diffusion–convection process during CO_2 storage in saline aquifers, Lawrence Berkeley National Laboratory, <http://www.escholarship.org/uc/item/2fc5v69p>, 2008.